Journal of Magnetics 31(1), 21-34 (2026)

ISSN (Print) 1226-1750
ISSN (Online) 2233-6656
https://doi.org/10.4283/JMAG.2026.31.1.21

Evaluation of Spin-Orbit Torque Efficiency in Ta/CoFeB Bilayers with Out-of-Plane and In-Plane Magnetizations Using Harmonic Hall Measurements

Hongwon Jeon[1†], Heungrae Cho[1†], Seongjong Yoon[1], Gunwoo Jung[1], Daeun Woo[1], San Ko[2], So young Shin[3], Kab-Jin Kim[2], Byong-Guk Park[3], and Soogil Lee[1*]

[1]*Department of Semiconductor Engineering, Gachon University, Seongnam 13120, Republic of Korea*
[2]*Department of Physics, Korea Advanced Institute of Science and Technology (KAIST), Daejeon 34141, Republic of Korea*
[3]*Department of Materials Science and Engineering, Korea Advanced Institute of Science and Technology (KAIST), Daejeon 34141, Republic of Korea*

(Received 6 January 2026, Received in final form 18 March 2026, Accepted 18 March 2026)

Spin-orbit torque (SOT) offers efficient magnetization control using spin currents generated by the spin Hall effect and/or the Rashba-Edelstein effect through charge-to-spin conversion. Quantitative evaluation of the SOT efficiency is crucial for understanding charge-to-spin conversion and optimizing energy-efficient spintronic devices. We evaluate the SOT efficiency in Ta/CoFeB bilayers with different magnetic anisotropies using harmonic Hall measurements, which allow the extraction of damping-like and field-like effective magnetic fields. From these measurements, the effective spin Hall angle, corresponding to the charge-to-spin conversion ratio, is determined to quantify the SOT efficiency. The effective spin Hall angles are found to be −0.052±0.002 and −0.052±0.004 for the up and down magnetization states of the perpendicularly magnetized sample, respectively, and −0.051±0.001 for the in-plane magnetized sample. These results demonstrate that the SOT efficiency remains nearly identical, irrespective of magnetic anisotropy, when the same spin-current source (a 4-nm-thick Ta layer) is employed.

Keywords : spin-orbit torque, spin Hall effect, harmonic Hall measurement, spin Hall angle

1. Introduction

Spin-orbit torque (SOT) is an efficient way to control magnetization using spin currents generated by the spin Hall effect (SHE) and/or the Rashba-Edelstein effect (REE) through spin-orbit coupling (SOC) [1–6]. SOT has received significant attention because it can provide excellent device performance compared to spin-transfer torque (STT) in spintronic devices, such as magnetic random-access memory (MRAM) [3, 4, 7–10]. First, SOT devices provide better reliability compared to STT devices. For example, STT-driven MRAM has a two-terminal structure, where the write and read paths share the same line. In this structure, the spin current is generated by spin filtering through charge current injection into the ferromagnet (FM)/tunnel barrier [7–9]. This increases the risk of tunnel barrier breakdown when a high current passes during writing. In contrast, SOT-driven MRAM has a three-terminal structure, where the write and read paths are separated [10–12]. The spin current is generated in the non-magnet (NM) layer or at the NM/FM interface without the need for it to pass through the tunnel barrier, thereby providing higher reliability. Second, SOT devices offer faster writing speeds. STT-driven MRAM requires an incubation time during switching due to the parallel or antiparallel alignment between the injected spin angular momentum and the magnetization. In contrast, SOT-driven MRAM does not require an incubation time because the injected spin angular momentum and the magnetization are orthogonal [12]. Therefore, there have been many efforts to find NM materials that exhibit a lower switching current with a large SOT efficiency [5, 6, 10, 13–15]. For this reason, the quantification of the SOT efficiency in various materials is crucial for developing SOT-based spintronic devices.

Conventionally, SOT is studied in NM/FM bilayers. In

[†] These authors contributed equally to this work.

*Corresponding author: Tel: +82-31-750-5564
e-mail: leesoogil83@gachon.ac.kr

these structures, a longitudinal charge current along the x-direction generates a transverse spin current along the z-direction, carrying polarized spin angular momentum ($\hat{s}$) along the y-direction through SHE and/or REE [5, 6, 10, 13–15]. SOT efficiency is determined by the ratio of charge-to-spin conversion, which is referred to as the spin Hall angle (θ_{SH}) [5, 6, 10, 13–15]. To evaluate θ_{SH}, it is necessary to quantify the strength of the effective magnetic fields generated by SOT. Two types of effective magnetic fields can be considered: the damping-like effective magnetic field (H_{DL}), which is along the direction of ($\hat{s} \times \hat{m}$), and the field-like effective magnetic field (H_{FL}), which is along the spin polarization direction $\hat{s}$. Here, $\hat{m}$ is the unit vector of the magnetization. There are several methods to obtain the effective magnetic fields based on changes in magnetization direction under SOT, such as harmonic Hall measurements [16–22], spin torque ferromagnetic resonance (ST-FMR) measurements [23–27], hysteresis loop shift measurements [28], and magnetization switching [29–31]. Among them, the harmonic Hall measurement is widely utilized to evaluate the SOT efficiency. This technique is based on magnetization oscillations and the associated Hall voltage change induced by applying an AC current. The harmonic Hall measurement can be applied to both out-of-plane and in-plane magnetizations. It is expected that the SOT efficiency should be consistent within an identical bilayer, regardless of the magnetic anisotropy, because the source of spin current is the identical NM and/or NM/FM interface. This consistency is crucial for two reasons. First, a reliable determination of θ_{SH} enables the systematic discovery of materials with high SOT efficiency. Second, a consistent evaluation of θ_{SH} is essential for the reliable implementation of SOT in MRAM and related spintronic devices.

In this Article, we compare the SOT efficiency obtained from different magnetic anisotropies. This Article consists of two parts. First, we derive the Hall voltage changes under SOT by applying an AC current. Second, we perform harmonic Hall measurements on both out-of-plane and in-plane magnetizations. Note that Ta/CoFeB bilayers were employed in all measurements. The thickness of Ta is the same in all samples, while that of CoFeB varies to control the magnetic anisotropy. The obtained θ_{SH} is -0.052 ± 0.002 (for the up magnetization state) and -0.052 ± 0.004 (for the down magnetization state) for out-of-plane magnetized CoFeB, and -0.051 ± 0.001 for in-plane magnetized CoFeB. These results clearly indicate that variations in magnetic anisotropy do not significantly affect θ_{SH}, even when different harmonic Hall measurement configurations are employed. Our findings demonstrate that harmonic Hall measurements provide a reliable and efficient method to quantify the SOT efficiency, independent of the magnetic anisotropy, provided that the spin current source remains identical.

2. The Effect of the Oscillatory Motion of Magnetization under Spin-Orbit Torque on Hall Resistances with an AC Current

We first examine the effect of magnetization oscillation under SOT on the Hall resistance by applying an AC current. In the NM/FM bilayer, the SOT induces a perturbation in the magnetization direction because the SOT can be regarded as the effective magnetic field. Consequently, this perturbation gives rise to changes in the Hall resistance (R_{xy}), originating from two contributions: the anomalous Hall effect (AHE), which reflects the change in the out-of-plane magnetization, and the planar Hall effect (PHE), which originates from that in the in-plane magnetization. To experimentally quantify these SOT-induced changes in R_{xy}, harmonic Hall measurements can be employed [16, 18–22]. In the following, we derive how the effective magnetic fields generated by the SOT contribute to the R_{xy} signals, based on the magnetization dynamics under either perpendicular magnetic anisotropy (PMA) or in-plane magnetic anisotropy (IMA).

Before deriving the R_{xy} expression under the perturbation, it is necessary to define the magnetization vector $\vec{M}$ and the external magnetic field vector $\vec{H}_{\mathrm{ext}}$, as shown in Figs. 1(a)-1(c). In this framework, θ and φ represent the polar and azimuthal angles of $\vec{M}$, respectively. $\vec{M}$ is defined as follows:

$$\vec{M} = M_{\mathrm{S}}\hat{m} \tag{1}$$

where M_{S} is the saturation magnetization, and $\hat{m}$ is the unit vector of magnetization. The x-, y-, and z-components of $\hat{m}$ are expressed by $\sin\theta\cos\varphi$, $\sin\theta\sin\varphi$, and $\cos\theta$, respectively:

$$\hat{m} = (\sin\theta\cos\varphi,\ \sin\theta\sin\varphi,\ \cos\theta) \tag{2}$$

$\vec{H}_{\mathrm{ext}}$ can also be expressed in terms of its directional angles as follows:

$$\vec{H}_{\mathrm{ext}} = H(\sin\theta_H\cos\varphi_H,\ \sin\theta_H\sin\varphi_H,\ \cos\theta_H) \tag{3}$$

where θ_H and φ_H represent the polar and azimuthal angles of $\vec{H}_{\mathrm{ext}}$, respectively. H indicates the magnitude of $\vec{H}_{\mathrm{ext}}$. Due to magnetic anisotropy, $\vec{M}$ does not perfectly align with the direction of $\vec{H}_{\mathrm{ext}}$. Therefore, θ and φ do not coincide with θ_H and φ_H. Under $\vec{H}_{\mathrm{ext}}$, $\vec{M}$ aligns to an

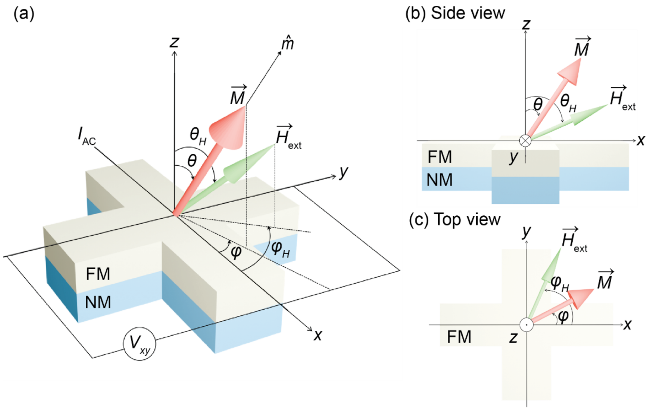

Fig. 1. (Color online) (a) Schematic illustration of the harmonic Hall measurement setup. An AC current is applied along the x-direction in the non-magnet (NM)/ferromagnet (FM) bilayer structure, while the magnetization vector $\vec{M}$ is defined by the polar angle θ and the azimuthal angle φ. The external magnetic field $\vec{H}_{\rm ext}$ is applied at a defined angle to set the magnetization orientation, allowing the measurement of SOT-induced perturbations via harmonic Hall resistances. (b) Side view (xz-plane) of the coordinate system, illustrating the polar angle θ of $\vec{M}$ and the polar angle θ_H of $\vec{H}_{\rm ext}$ with respect to the z-axis. This geometry is used to describe the out-of-plane components of $\vec{M}$ and $\vec{H}_{\rm ext}$. (c) Top view (xy-plane) of the coordinate system, showing the azimuthal angle φ of the magnetization vector $\vec{M}$ and the azimuthal angle φ_H of the external magnetic field $\vec{H}_{\rm ext}$ with respect to the x-axis. This configuration is used to define the in-plane orientations of M and H during field rotations.

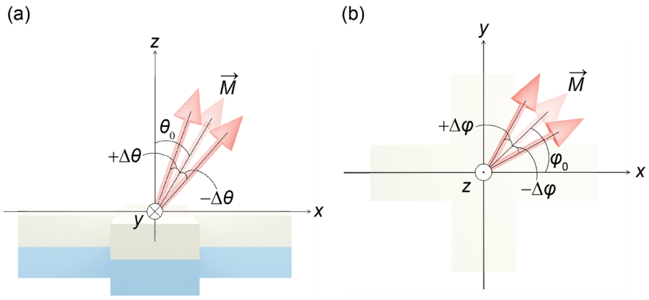

Fig. 2. (Color online) (a) Schematic illustration of the polar angular deviation $\Delta\theta$ of the magnetization vector $\vec{M}$ with respect to the z-axis in the xz-plane. (b) Schematic illustration of the azimuthal angular deviation $\Delta\varphi$ of $\vec{M}$ with respect to the x-axis in the xy-plane. These angular deviations are induced by spin–orbit torque and form the basis for the analysis of harmonic Hall resistance signals.

equilibrium orientation determined by angles of θ_0 and φ_0.

When SOT is introduced, the magnetization slightly deviates from its equilibrium (θ_0 and φ_0), resulting in small angular deviations of $\Delta\theta$ and $\Delta\varphi$, as shown in Fig. 2. The sign of these deviations depends on the direction of the effective magnetic fields generated by SOT. $\Delta\theta$ and $\Delta\varphi$ can be expressed as:

$$\Delta\theta = \frac{\partial\theta}{\partial H_x}\Delta H_x + \frac{\partial\theta}{\partial H_y}\Delta H_y + \frac{\partial\theta}{\partial H_z}\Delta H_z \tag{4}$$

$$\Delta\varphi = \frac{\partial\varphi}{\partial H_x}\Delta H_x + \frac{\partial\varphi}{\partial H_y}\Delta H_y + \frac{\partial\varphi}{\partial H_z}\Delta H_z \tag{5}$$

where $\frac{\partial\theta}{\partial H_i}$ and $\frac{\partial\varphi}{\partial H_i}$ represent the angular susceptibilities with respect to an applied magnetic field component ΔH_i ($i = x$, y, and z), quantifying how much θ and φ vary in response to each field direction. The terms ΔH_x, ΔH_y, and ΔH_z represent the effective magnetic fields generated by the SOT along the x-, y-, and z-directions, respectively. To obtain $\frac{\partial\theta}{\partial H_i}$ and $\frac{\partial\varphi}{\partial H_i}$, it is necessary to define the magnetic potential energy E, which can be expressed as the sum of the anisotropy energy and the Zeeman energy:

$$E = -K_\perp\cos^2\theta - K_\parallel\sin^2\theta\sin^2\varphi - \vec{M}\cdot\vec{H}_{\rm ext} \tag{6}$$

where $K_\perp$ and $K_\parallel$ represent the out-of-plane (perpendicular) and in-plane easy-axis anisotropy energy constants, respectively. The first and second terms correspond to the magnetic anisotropy energies. The third term represents the Zeeman energy. Based on Eq. (6), the equilibrium magnetization direction (θ_0, φ_0) can be obtained by applying the conditions $\frac{\partial E}{\partial\theta} = 0$ and $\frac{\partial E}{\partial\varphi} = 0$:

$$\begin{aligned}\frac{\partial E}{\partial\theta} = 0 = &\left(K_\perp - K_\parallel\sin^2\varphi_0\right)\sin 2\theta_0 \\ &- M_{\rm S}H\begin{bmatrix}\cos\theta_0\sin\theta_H\left(\cos\varphi_0\cos\varphi_H + \sin\varphi_0\sin\varphi_H\right) \\ -\sin\theta_0\cos\theta_H\end{bmatrix}\end{aligned} \tag{7}$$

$$\begin{aligned}\frac{\partial E}{\partial\varphi} = 0 = &-K_\parallel\sin^2\theta_0\sin 2\varphi_0 \\ &- M_{\rm S}H\sin\theta_0\sin\theta_H\sin\left(\varphi_H - \varphi_0\right)\end{aligned} \tag{8}$$

By differentiating Eqs. (7) and (8) with respect to H_i, the angular response of the magnetization to small perturbations in the external field can be described by two coupled linear equations for $\frac{\partial\theta}{\partial H_i}$ and $\frac{\partial\varphi}{\partial H_i}$:

$$\begin{aligned}\frac{\partial}{\partial H_i}\left(\frac{\partial E}{\partial\theta}\right) = 0 = &[\left(K_\perp - K_\parallel\sin^2\varphi_0\right)2\cos 2\theta_0 - M_{\rm S}(-H_x\sin\theta_0\cos\varphi_0 \\ &-H_y\sin\theta_0\sin\varphi_0 - H_z\cos\theta_0)]\frac{\partial\theta}{\partial H_i} + [-K_\parallel\sin 2\theta_0\sin 2\varphi_0 \\ &- M_{\rm S}\cos\theta_0(-H_x\sin\varphi_0 + H_y\cos\varphi_0)]\frac{\partial\varphi}{\partial H_i} - M_{\rm S}\frac{\partial\hat{m}}{\partial\theta}\end{aligned} \tag{9}$$

$$\begin{aligned}\frac{\partial}{\partial H_i}\left(\frac{\partial E}{\partial \varphi}\right) &= 0 = [-K_{\parallel}\sin 2\theta_0 \sin 2\varphi_0 + M_{\mathrm{S}}\cos\theta_0 \\ &(H_x \sin\varphi_0 - H_y\cos\varphi_0)]\frac{\partial\theta}{\partial H_i} + [-2K_{\parallel}\sin^2\theta_0\cos 2\varphi_0 \\ &+ M_{\mathrm{S}}\sin\theta_0 (H_x\cos\varphi_0 + H_y\sin\varphi_0)]\frac{\partial\varphi}{\partial H_i} - M_{\mathrm{S}}\frac{\partial\hat{m}}{\partial\varphi}\end{aligned} \tag{10}$$

Here, H_x, H_y, and H_z denote the Cartesian components of the H_i:

$$H_x = H\sin\theta_H\cos\varphi_H,\ H_y = H\sin\theta_H\sin\varphi_H,\ H_z = H\cos\theta_H \tag{11}$$

The partial derivatives of $\hat{m}$ with respect to θ and φ are given as:

$$\frac{\partial\hat{m}}{\partial\theta} = \left[\cos\theta_0\cos\varphi_0,\ \cos\theta_0\sin\varphi_0,\ -\sin\theta_0\right] \tag{12}$$

$$\frac{\partial\hat{m}}{\partial\varphi} = \left[\sin\theta_0\sin\varphi_0,\ -\sin\theta_0\cos\varphi_0,\ 0\right] \tag{13}$$

Substituting Eqs. (11), (12), and (13) into Eqs. (9) and (10), and subsequently inserting these results into Eqs. (4) and (5), yields the final expressions for $\Delta\theta$ and $\Delta\varphi$ as follows:

$$\Delta\theta = \frac{\cos\theta_0\left(\Delta H_x\cos\varphi_H + \Delta H_y\sin\varphi_H\right) - \sin\theta_0\Delta H_z}{H_K\cos 2\theta_0 + H\cos\left(\theta_H - \theta_0\right)} \tag{14}$$

$$\Delta\varphi = \frac{-\Delta H_x\sin\varphi_H + \Delta H_y\cos\varphi_H}{H\sin\theta_H} \tag{15}$$

where H_K represents the PMA field, defined as:

$$H_K \equiv \frac{2K_{\perp}}{M_{\mathrm{S}}} \tag{16}$$

The angular deviations $\Delta\theta$ and $\Delta\varphi$ are directly related to changes in the Hall resistances arising from the AHE and PHE, because these angular modulations represent out-of-plane and in-plane magnetization oscillations, respectively, which directly influence the R_{xy} signal. To quantify the angular dependence, R_{xy} can be expressed as a function of the magnetization angles (θ, φ), incorporating contributions from both the AHE and the PHE [18, 20, 22], as given by:

$$R_{xy} = \frac{1}{2}\Delta R_{\mathrm{AHE}}\cos\theta + \frac{1}{2}\Delta R_{\mathrm{PHE}}\sin^2\theta\sin 2\varphi \tag{17}$$

where ΔR_{AHE} and ΔR_{PHE} are the R_{xy} changes due to the AHE and PHE, respectively. Fig. 3 shows the typical R_{xy} characteristics for Hall-bar-patterned samples with PMA and IMA systems. The film stacks were deposited by DC and RF magnetron sputtering on 300-nm-thick thermally oxidized SiO_2 substrates, consisting of Ta (4.0 nm)/$Co_{32}Fe_{48}B_{20}$ (1.2 nm) for the PMA system and Ta (4.0 nm)/$Co_{32}Fe_{48}B_{20}$ (2 nm) for the IMA system. All samples were capped with MgO (2 nm)/Ta (2 nm) to prevent oxidation. Hall bars with a channel width of 5 μm and a length of 25 μm were fabricated using photolithography and Ar ion milling for electrical measurements. Figs. 3(a)-3(c) correspond to the PMA system and Figs. 3(d)-(f) correspond to the IMA system.

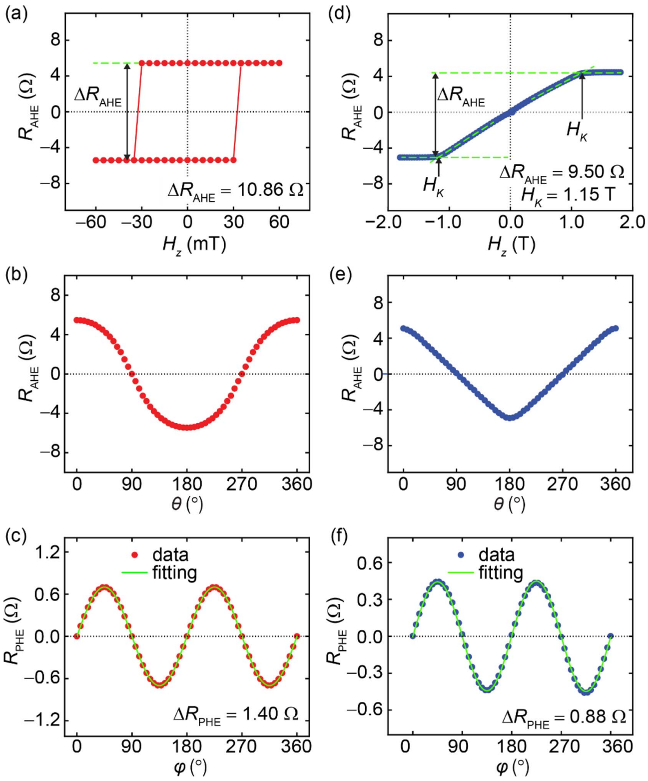

Fig. 3. (Color online) Representative Hall measurement results for perpendicular magnetic anisotropy (PMA) and in-plane magnetic anisotropy (IMA) systems. For the PMA system: (a) the anomalous Hall resistance (R_{AHE}) as a function of out-of-plane magnetic field (H_z), (b) the R_{AHE} as a function of the polar angle θ obtained from the polar rotation scans, and (c) the planar Hall resistance (R_{PHE}) as a function of the azimuthal angle φ. For the IMA system: (d) the R_{AHE} as a function of H_z, (e) the R_{AHE} as a function of the θ, and (f) the R_{PHE} as a function of the φ.

For the PMA system, as shown in Fig. 3(a), ΔR_{AHE} obtained by sweeping the external magnetic field H_z exhibits a square-like hysteresis loop, indicating clear magnetization switching between the up and down states. The difference between the saturated resistances in the up and down magnetization states gives the anomalous Hall resistance change, expressed as $\Delta R_{\mathrm{AHE}} = R_{\mathrm{AHE}}(+M_z) - R_{\mathrm{AHE}}(-M_z) = 10.86\ \Omega$. Fig. 3(b) represents R_{AHE} as a function of θ, measured under an external magnetic field of 3 T. The data exhibit an overall $\cos\theta$-like trend consistent with the first term of Eq. (17), although slight deviations are observed due to the planar Hall contribution and finite magnetization tilting during rotation. Fig. 3(c) shows R_{PHE} as a function of the azimuthal angle φ for $\theta = 90°$, measured under an external field of 3 T. The experimental R_{PHE} data follow a $\sin 2\varphi$ dependence, consistent with the second term of Eq. (17) and the measured ΔR_{PHE} is 1.40 Ω.

For the IMA system, as shown in Fig. 3(d), R_{AHE} as a function of H_z shows the hard-axis response. To extract H_K experimentally, the H_z versus R_{AHE} curve is analyzed by performing linear fittings to the saturated regions of the curve for both positive and negative fields separately. The intersection points of the two fitted lines correspond to H_K. The final H_K value is obtained by averaging the intersection points determined from the positive and negative fields. Consequently, the extracted H_K value is 1.15 T for the IMA system. The anomalous Hall resistance change was similarly obtained from the difference between the two saturated resistance values, giving $\Delta R_{\mathrm{AHE}} = 9.50\ \Omega$. Fig. 3(e) displays the R_{AHE} dependence measured under an external magnetic field of 3 T. The data show a $\cos\theta$-like trend characteristic of the AHE, with minor deviations likely originating from the PHE. Fig. 3(f) presents R_{PHE} as a function of φ at $\theta = 90°$, measured under an external magnetic field of 2 T. The data follow a $\sin 2\varphi$ dependence, consistent with the second term of Eq. (17), and the measured ΔR_{PHE} is 0.88 Ω.

In the equilibrium state under the influence of SOT, the magnetization direction can be expressed as $\theta = \theta_0 + \Delta\theta$ and $\varphi = \varphi_0 + \Delta\varphi$, with the assumptions $\Delta\theta << 1°$ and $\Delta\varphi << 1°$. Under this small-angle approximation, substituting $\theta = \theta_0 + \Delta\theta$ and $\varphi = \varphi_0 + \Delta\varphi$ into Eq. (17) gives:

$$R_{xy} \approx \frac{1}{2}\Delta R_{\mathrm{AHE}}\left(\cos\theta_0 - \Delta\theta\sin\theta_0\right) + \frac{1}{2}\Delta R_{\mathrm{PHE}}\left(\sin^2\theta_0 + \Delta\theta\sin 2\theta_0\right)\left(\sin 2\varphi_0 + 2\Delta\varphi\cos 2\varphi_0\right) \tag{18}$$

Next, we consider $R_{xy} = V_{xy}/I$ with the AC current $I = \Delta I \sin(\omega t)$, where $\omega = 2\pi f$ denotes the angular frequency corresponding to the frequency f, and t is time. Here, ΔI represents the amplitude of the applied AC current. When f is sufficiently low (e.g., ~10 Hz) compared to the typical ferromagnetic resonance condition (e.g., ~GHz), the angular deviations $\Delta\theta$ and $\Delta\varphi$ induced by the SOT are synchronized with f, allowing them to be detected in the measured R_{xy}. In this case, the angular deviations can be expressed as $\Delta\theta = \Delta\theta\sin(\omega t)$ and $\Delta\varphi = \Delta\varphi\sin(\omega t)$. Substituting these AC-current-dependent expressions into Eq. (18) yields the following time-dependent form of R_{xy}:

$$R_{xy} = R_0 + R_{1\omega}\sin(\omega t) + R_{2\omega}\cos(2\omega t) \tag{19}$$

where R_0, $R_{1\omega}$, and $R_{2\omega}$ represent the DC, first harmonic, and second harmonic components of the Hall resistance, respectively. These components can be written as:

$$R_0 = \frac{1}{2}\begin{bmatrix} \frac{1}{2}\left(-\Delta R_{\mathrm{AHE}}\sin\theta_0 + \Delta R_{\mathrm{PHE}}\sin 2\theta_0 2\varphi_0\right)\Delta\theta \\ +\Delta R_{\mathrm{AHE}}\sin^2\theta_0\cos 2\varphi_0\Delta\varphi \end{bmatrix} \tag{20}$$

$$R_{1\omega} = \frac{1}{2}\Delta R_{\mathrm{AHE}}\cos\theta_0 + \frac{1}{2}\Delta R_{\mathrm{PHE}}\sin^2\theta_0\sin 2\varphi_0 \tag{21}$$

$$R_{2\omega} = -\frac{1}{2}\begin{bmatrix} \frac{1}{2}\left(-\Delta R_{\mathrm{AHE}}\sin\theta_0 + \Delta R_{\mathrm{PHE}}\sin 2\theta_0\sin 2\varphi_0\right)\Delta\theta \\ +\Delta R_{\mathrm{AHE}}\sin^2\theta_0\cos 2\varphi_0\Delta\varphi \end{bmatrix} \tag{22}$$

Here, R_0 corresponds to the static Hall resistance determined under equilibrium magnetization. The first harmonic component $R_{1\omega}$ represents the equilibrium response governed by the external magnetic field $\vec{H}_{\mathrm{ext}}$. The second harmonic component $R_{2\omega}$ originates from the nonlinear modulation of the magnetization induced by the SOT. Although the Hall resistance is obtained by dividing the measured Hall voltage by the applied current, the time dependence originating from the AC current remains inherent in the resistance terms. Consequently, $R_{xy}(\omega t)$ inherently exhibits a periodic modulation of the magnetization synchronized with the instantaneous current $I(\omega t) = \Delta I\sin(\omega t)$. Therefore, even after dividing by the current amplitude ΔI, the residual sinusoidal dependence $\sin(\omega t)$ is preserved in $R_{xy}(\omega t)$, leading to the emergence of both first and second harmonic components in the measured resistance. Since the resistance $R_{xy}(\omega t)$ also oscillates with time due to the magnetization modulation induced by the SOT, their product contains a nonlinear term $I(\omega t)^2$. This nonlinearity arises from the mixing between the driving current that generates the effective fields and the probing current used to detect the Hall voltage. When an AC current $\Delta I \sin(\omega t)$ is applied, this nonlinearity produces a term $\sin(\omega t) \times \sin(\omega t)$, which can be rewritten as $\frac{1-\cos(2\omega t)}{2}$, containing a DC component and a 2ω component. Consequently, SOT-related signals predominantly appear in the $R_{2\omega}$.

To understand the effect of spin torques on the magnetization dynamics, we consider the Landau–Lifshitz–Gilbert

(LLG) equation [32, 33], which describes the dynamics of $\vec{M}$ under an effective magnetic field $\vec{H}_{\text{ext}}$:

$$\frac{\partial \vec{M}}{\partial t} = -\gamma \vec{M} \times \vec{H}_{\text{ext}} + \frac{\alpha}{M_{\text{S}}} \vec{M} \times \frac{\partial \vec{M}}{\partial t} \tag{23}$$

where γ is the gyromagnetic ratio, and α is the Gilbert damping constant. The first term corresponds to the precession of the magnetization around $\vec{H}_{\text{ext}}$, while the second term represents the damping process that aligns $\vec{M}$ with $\vec{H}_{\text{ext}}$. $\vec{H}_{\text{ext}}$ consists of multiple contributions, including $\vec{H}_{\text{ext}}$, magnetic anisotropy field $\vec{H}_{\text{ani}}$, and additional fields such as those induced by SOT. By rearranging Eq. (23), the LLG equation can be expressed in a form that separates the precession and damping terms, which is particularly useful when incorporating additional spin torque terms. The resulting expression is:

$$\frac{\partial \vec{M}}{\partial t} = \frac{\gamma}{1+\alpha^2} \vec{H}_{\text{ext}} \times \vec{M} + \frac{\gamma\alpha}{(1+\alpha^2) M_{\text{S}}} \vec{M} \times (\vec{H}_{\text{ext}} \times \vec{M}) \tag{24}$$

The SOT originates from the interaction between the spin polarization vector $\hat{s}$, generated by the SHE and/or the REE, and the magnetization vector $\hat{m}$ of the FM. For symmetry and conservation considerations (i.e., the torque must correspond to a pure rotation of a fixed-length magnetization and thus be transverse to $\hat{m}$), the torque acting on the FM is always perpendicular to $\hat{m}$ [33]. Within the LLG framework, where $|\hat{m}| = 1$, only a torque perpendicular to $\hat{m}$ can change its direction without changing its magnitude. Any torque (τ) component parallel to $\hat{m}$ would yield $\hat{m} \cdot \tau \neq 0$, which would alter the magnetization magnitude rather than its direction, and is thus not allowed under the fixed-length magnetization assumption. Consequently, the most general torque form can be constructed from two mutually orthogonal basis vectors involving $\hat{s}$ and $\hat{m}$, both inherently perpendicular to $\hat{m}$: the field-like basis vector ($\hat{s} \times \hat{m}$) and the damping-like basis vector $\hat{m} \times (\hat{s} \times \hat{m})$. Therefore, the spin-orbit torque τ_{SOT} can be generally expressed as:

$$\tau_{\text{SOT}} = \tau_{\text{FL}} (\hat{s} \times \hat{m}) + \tau_{\text{DL}} \hat{m} \times (\hat{s} \times \hat{m}) \tag{25}$$

This expression shows that the SOT consists of two distinct components: the field-like torque (τ_{FL}) and the damping-like torque (τ_{DL}). τ_{FL} typically causes the magnetization to precess around $\hat{s}$, whereas τ_{DL} tends to align or anti-align the magnetization with $\hat{s}$, leading to magnetization damping or switching [3, 4, 6]. By comparing this SOT expression with the LLG equation, one can see a structural similarity. If $\vec{H}_{\text{ext}}$ is replaced by $\hat{s}$, then τ_{FL} corresponds to the precession term, and τ_{DL} corresponds to the damping term in the LLG equation.

3. Determination of the Effective Spin Hall Angle from Effective Fields

Next, we examine the connection between the strength of the SOT effective fields and the spin Hall angle (θ_{SH}). The θ_{SH} is defined as the ratio of the spin current density (j_{s}) to the charge current density (j_{c}):

$$\theta_{\text{SH}} = \frac{j_{\text{s}}}{j_{\text{c}}} \tag{26}$$

However, in practice, not all of the spin current contributes to the torque on the FM layer, due to spin relaxation and spin backflow at the NM/FM interface [27, 34–37]. These interfacial losses are described by the interfacial spin transparency ($0 \le T_{\text{int}} \le 1$). Consequently, the experimentally observed torque is proportional to $T_{\text{int}} \cdot j_{\text{s}}$, and the measured θ_{SH} derived from torque efficiency inherently includes this T_{int}. To address this, we define the effective spin Hall angle ($\theta_{\text{SH}}^{\text{eff}}$) as:

$$\theta_{\text{SH}}^{\text{eff}} = T_{\text{int}} \cdot \theta_{\text{SH}} \tag{27}$$

This $\theta_{\text{SH}}^{\text{eff}}$ can be determined using the following relation:

$$\theta_{\text{SH}}^{\text{eff}} = \frac{\left(\frac{2e}{\hbar}\right) M_{\text{S}} t_{\text{FM}} H_{\text{DL}}}{j_{\text{NM}}} \tag{28}$$

where e is the electron charge, $\hbar$ is the reduced Planck constant, t_{FM} is the thickness of the FM, and j_{NM} is the current density in the NM [6]. Eq. (28) provides a direct quantitative link between the angular momentum transfer from the spin current to the magnetization dynamics of the FM layer. The prefactor $\frac{2e}{\hbar}$ serves as the conversion factor between charge current and spin angular momentum, $M_{\text{S}} t_{\text{FM}}$ defines the total magnetic moment subjected to the torque, and H_{DL} denotes the damping-like effective field, corresponding to the strength of the spin current component perpendicular to the magnetization. Harmonic Hall measurements enable the determination of both H_{FL} and H_{DL}. Since τ_{DL} is typically associated with the bulk SHE in the NM layer, the magnitude of H_{DL} provides a direct measure of spin Hall efficiency and allows for the estimation of $\theta_{\text{SH}}^{\text{eff}}$ [6, 38]. The procedures for determining both H_{DL} and H_{FL} in bilayers with PMA and IMA will be discussed in detail in the following sections.

4. Effective Fields of SOT in PMA Systems

In this section, we examine harmonic measurements in a perpendicularly magnetized CoFeB system. First, we derive the 1st and 2nd harmonic resistances in bilayer systems with PMA. When a small in-plane external magnetic field is applied along the *xy*-plane (θ_H = 90°), the polar angle variation of the magnetization vector is negligibly small ($\theta_0 < 1°$) due to the strong PMA. Thus, we can approximate $\sin\theta_0 \sim \theta_0$ and $\cos\theta_0 \sim 1 - (\theta_0)^2/2$. Under the same condition, the azimuthal angle φ_0 aligns with the in-plane direction of the external magnetic field, i.e., $\varphi_0 = \varphi_H$. Under these approximations, Eq. (7) can be rewritten as:

$$\begin{aligned}\frac{\partial E}{\partial\theta} &= 0 = (K_\perp - K_\parallel \sin^2\varphi_H)2\theta_0 \\ &\quad - M_S H[\sin\theta_H(\cos\varphi_H\cos\varphi_H + \sin\varphi_H\sin\varphi_H) - \theta_0\cos\theta_H]\end{aligned} \tag{29}$$

Here, the in-plane anisotropy constant is defined as $K_\parallel \equiv \frac{H_A M_S}{2}$, where H_A denotes the in-plane anisotropy field. Since H_A is assumed to be negligible, the term $K_\parallel \sin^2\varphi_H$ in Eq. (29) can be ignored. By substituting Eq. (16) into Eq. (29) under this condition, we obtain:

$$\theta_0 = \frac{H\sin\theta_H}{H_K \pm H\cos\theta_H}, \quad \varphi_0 = \varphi_H \tag{30}$$

where ± symbols correspond to the up ($\vec{M}//+z$) and down ($\vec{M}//-z$) magnetization states, respectively. By substituting Eq. (30) into the general modulation relations of the magnetization angles given in Eqs. (14) and (15) for $\Delta\theta$ and $\Delta\varphi$, respectively, the expressions for the $R_{1\omega}$ and $R_{2\omega}$ in Eqs. (21) and (22) can be reformulated for the PMA configuration. As a result, the harmonic resistances can be expressed as:

$$R_{1\omega} \approx \pm\frac{1}{2}\Delta R_{\mathrm{AHE}}\left[1 - \frac{1}{2}\left(\frac{H\sin\theta_H}{H_K \pm H\cos\theta_H}\right)^2\right] \tag{31}$$

$$\begin{aligned}R_{2\omega} &\approx -\frac{1}{4}\begin{bmatrix}\mp\Delta R_{\mathrm{AHE}}\left(\Delta H_x\cos\varphi_H + \Delta H_y\cos\varphi_H\right) \\ +2\Delta R_{\mathrm{PHE}}\left(-\Delta H_x\sin\theta_H + \Delta H_y\cos\theta_H\right)\cos 2\varphi_H\end{bmatrix} \\ &\quad\times\frac{H\sin\theta_H}{\left(H_K \pm H\cos\theta_H\right)^2}\end{aligned} \tag{32}$$

As shown in Eq. (31), the first harmonic resistance is primarily governed by the anomalous Hall contribution. This occurs because the planar Hall contribution is proportional to $\sin^2\theta_0 \sim (\theta_0)^2$, which is strongly suppressed under the small angle approximation ($\theta_0 < 1°$). Therefore, the PHE term effectively vanishes in $R_{1\omega}$, leaving the AHE term as the dominant contribution. In Eq. (32), the $R_{2\omega}$ is obtained by substituting Eq. (30) and incorporating the small perturbations $\Delta\theta$ and $\Delta\varphi$ defined in Eqs. (14) and (15). These results indicate that $R_{2\omega}$ is sensitive to both ΔH_x and ΔH_y, which represent the effective magnetic fields induced by SOT.

To eliminate the dependence of the $R_{1\omega}$ and $R_{2\omega}$ on the magnitude of the external magnetic field *H*, Eq. (31) is differentiated twice with respect to *H*, and Eq. (32) is differentiated once. By substituting θ_H = 90°, the following relations are obtained:

$$\frac{\partial^2 R_{1\omega}}{\partial H^2} \approx \mp\frac{\frac{1}{2}\Delta R_{\mathrm{AHE}}}{H_K^2} \tag{33}$$

$$\frac{\partial R_{2\omega}}{\partial H} \approx \frac{-\frac{1}{4}\begin{bmatrix}\mp\Delta R_{\mathrm{AHE}}\left(\Delta H_x\cos\varphi_H + \Delta H_y\sin\varphi_H\right) \\ +2\Delta R_{\mathrm{PHE}}\left(-\Delta H_x\sin\varphi_H + \Delta H_y\cos\varphi_H\right)\cos 2\varphi_H\end{bmatrix}}{H_K^2} \tag{34}$$

Eq. (33) shows that increasing H_K decreases the curvature of the first harmonic resistance $R_{1\omega}$, which is consistent with its quadratic dependence on the external magnetic field. Eq. (34) shows that the second harmonic resistance $R_{2\omega}$ varies linearly with the external magnetic field, demonstrating its direct proportionality to the SOT-induced effective fields ΔH_x and ΔH_y. To further analyze this behavior quantitatively, we define the ratio of derivatives (*B*) as:

$$\begin{aligned}B &\equiv \left(\frac{\partial R_{2\omega}}{\partial H} / \frac{\partial^2 R_{1\omega}}{\partial H^2}\right) = \\ &-\frac{1}{2}\begin{bmatrix}\left(\Delta H_x \mp 2\frac{\Delta R_{\mathrm{PHE}}}{\Delta R_{\mathrm{AHE}}}\cos 2\varphi_H \Delta H_y\right)\cos\varphi_H \\ +\left(\Delta H_y \pm 2\frac{\Delta R_{\mathrm{PHE}}}{\Delta R_{\mathrm{AHE}}}\cos 2\varphi_H \Delta H_x\right)\sin\varphi_H\end{bmatrix}\end{aligned} \tag{35}$$

For specific field orientations, φ_H = 0° ($\vec{H}_{\mathrm{ext}}//x$) and 90° ($\vec{H}_{\mathrm{ext}}//y$), Eq. (35) simplifies to:

$$B_x\left(\varphi_H = 0^\circ\right) = -\frac{1}{2}\left(\Delta H_x \mp 2\frac{\Delta R_{\mathrm{PHE}}}{\Delta R_{\mathrm{AHE}}}\Delta H_y\right) \tag{36}$$

$$B_y\left(\varphi_H = 90^\circ\right) = -\frac{1}{2}\left(\Delta H_y \mp 2\frac{\Delta R_{\mathrm{PHE}}}{\Delta R_{\mathrm{AHE}}}\Delta H_x\right) \tag{37}$$

From Eqs. (36) and (37), the SOT-induced effective

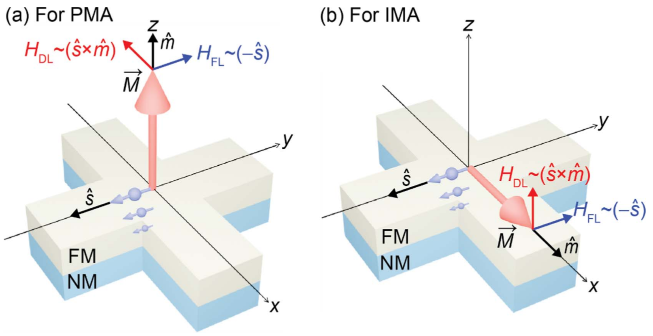

Fig. 4. (Color online) Schematic of the spin-orbit torque (SOT) directions in non-magnet (NM)/ferromagnet (FM) bilayer systems with (a) perpendicular magnetic anisotropy (PMA) and (b) in-plane magnetic anisotropy (IMA). The spin polarization vector ($\hat{s}$) is oriented along the $-y$-direction. Damping-like torque (τ_{DL}) and field-like torque (τ_{FL}) generate effective fields H_{DL} (~($\hat{s}\times\hat{m}$)) and H_{FL} (~ $-\hat{s}$), respectively.

fields ΔH_x and ΔH_y can be extracted as:

$$\Delta H_x = -2\frac{\left(B_x \pm 2\xi B_y\right)}{1-4\xi^2} \tag{38}$$

$$\Delta H_y = -2\frac{\left(B_y \pm 2\xi B_x\right)}{1-4\xi^2} \tag{39}$$

Here, $\xi = \Delta R_{PHE}/\Delta R_{AHE}$. As shown in Fig. 4(a), effective magnetic fields ΔH_x and ΔH_y correspond to the effective fields generated by the τ_{DL} and the τ_{FL}, respectively, as described in Eq. (25). Thus, ΔH_x and ΔH_y are identified as H_{DL} and H_{FL}, which represent the effective fields induced by SOT.

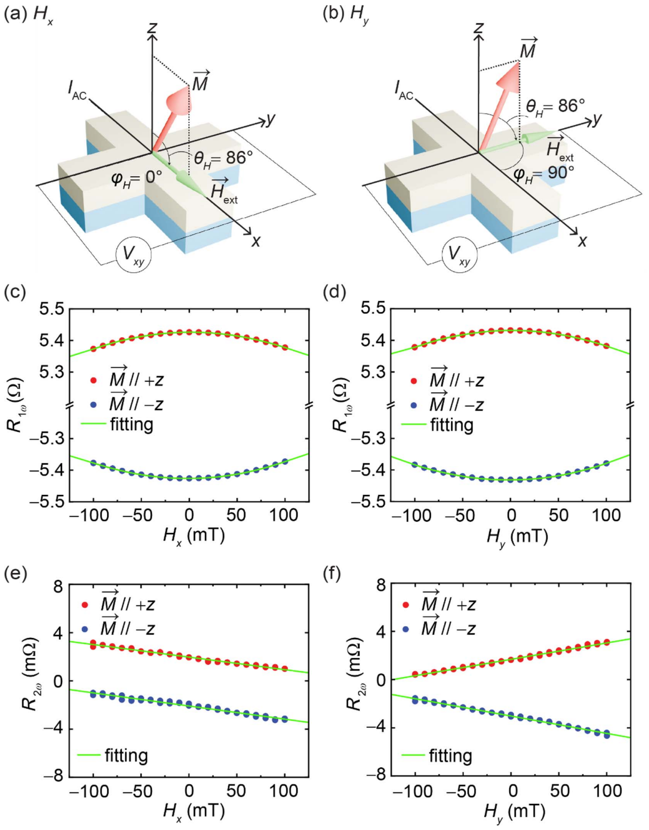

Fig. 5. (Color online) First and second harmonic Hall resistances ($R_{1\omega}$ and $R_{2\omega}$) for the Ta (4 nm)/CoFeB (1.2 nm) bilayer structure with perpendicular magnetic anisotropy. (a-b) Schematic illustrations of the harmonic Hall resistance measurement geometry: (a) the external magnetic field $\vec{H}_{ext}$ is applied along the x-axis (φ_H = 0°) and (b) the y-axis (φ_H = 90°). The polar angle of the applied field is fixed at θ_H = 86° to ensure single-domain formation. The magnetization $\vec{M}$ is slightly tilted from the out-of-plane direction under the external magnetic field. (c-d) $R_{1\omega}$ as a function of the external magnetic field applied along (c) the x-axis (H_x) and (d) the y-axis (H_y). The green curves indicate fitting lines based on Eq. (33). (e-f) $R_{2\omega}$ as a function of the external magnetic field applied along (e) the x-axis (H_x) and (f) the y-axis (H_y). The red and blue curves represent measurements under opposite magnetization states ($+M_z$ and $-M_z$), respectively. The green lines indicate fitting lines obtained from Eq. (34).

We next experimentally evaluate the effective fields in the Ta (4 nm)/$Co_{32}Fe_{48}B_{20}$ (1.2 nm) bilayer structure with PMA. As shown in Figs. 3(a)-3(c), the measured values of ΔR_{AHE} and ΔR_{PHE} are 10.86 Ω and 1.40 Ω. In the harmonic Hall measurements, the external magnetic field is applied at θ_H = 86° with φ_H = 0° and 90°, as shown in Figs. 5(a) and (b), respectively. Note that the external field is applied at a tilted polar angle (θ = 4°) to ensure a single-domain state. The sweeping range of the external magnetic field is set to ±100 mT which is smaller than the coercivity of CoFeB at this polar angle. Figs. 5(c) and 5(d) show the $R_{1\omega}$ when a magnetic field is applied along the x- and y-axes, respectively. Both curves exhibit identical behavior, reflecting the absence of a preferred in-plane direction. Furthermore, when the magnetization is aligned in the up and down states, the curves display opposite curvatures: negative for up state and positive for the down state, consistent with Eq. (33). Figs. 5(e) and 5(f) also present the $R_{2\omega}$ curves under external magnetic field sweeps along the x- and y-axes. During the H_x sweep, the direction of the effective field ΔH_x (H_{DL}) can be determined by considering Eq. (25) with Fig. 4(a). When the magnetization is in the up state, ΔH_x points toward the $-x$-direction, resulting in a negative slope in Eq. (40), substituting φ_H = 0° into Eq. (34). In contrast, when the magnetization is in the down state, ΔH_x switches to the $+x$-direction, but it still produces a negative slope in Eq. (40). This interpretation agrees with the observation in Fig. 5(e), where both the up and down magnetization states exhibit the same negative slope in $R_{2\omega}$ resistances.

$$\frac{\partial R_{2\omega}}{\partial H} \approx \frac{-\frac{1}{4}\left[\mp\Delta R_{\mathrm{AHE}}\left(\Delta H_x\right)+2\Delta R_{\mathrm{PHE}}\left(\Delta H_y\right)\right]}{H_K^2} \tag{40}$$

During the H_y sweep, the direction of the effective field ΔH_y (H_{FL}) can be determined by considering Eq. (25) together with Fig. 4(b). This H_{FL} is independent of the magnetization direction and is solely governed by the spin polarization direction $\hat{s}$. In both the up and down magnetization states, ΔH_y consistently points toward the $+y$-direction. Thus, the $R_{2\omega}$ resistance shows opposite trends: a positive slope for the up state and a negative slope for the down state, as described by Eq. (41), obtained by substituting $\varphi_H = 90°$ into Eq. (34). This interpretation is fully consistent with the experimental results shown in Fig. 5(f).

$$\frac{\partial R_{2\omega}}{\partial H} \approx \frac{-\frac{1}{4}\left[\mp\Delta R_{\mathrm{AHE}}(\Delta H_y)-2\Delta R_{\mathrm{PHE}}(-\Delta H_x)\right]}{H_K^2} \tag{41}$$

To quantitatively extract the effective fields from experimental results, we analyze the curvature and slope of the harmonic resistance curves. Using Eqs. (36) and (37), the ratios between curvature and slope are calculated. For the up magnetization state, the extracted values are $B_x = 1.98 \pm 0.05$ mT and $B_y = -2.50 \pm 0.13$ mT, while for the down magnetization state, $B_x = -2.16 \pm 0.08$ mT and $B_y = -3.12 \pm 0.17$ mT. Substituting these values into Eqs. (38) and (39) yields the H_{DL} and H_{FL}. For the up magnetization state, $H_{\mathrm{DL}} = -2.85 \pm 0.13$ mT and $H_{\mathrm{FL}} = 4.25 \pm 0.29$ mT are obtained, whereas for the down magnetization state, $H_{\mathrm{DL}} = 2.86 \pm 0.19$ mT and $H_{\mathrm{FL}} = 5.49 \pm 0.37$ mT are determined.

The extracted H_{DL} values are substituted into Eq. (28) to evaluate the $\theta_{\mathrm{SH}}^{\mathrm{eff}}$. Using the saturation magnetization of $M_{\mathrm{S}} = 4.02 \times 10^5$ A/m, obtained from vibrating sample magnetometer (VSM) measurements, and applying a current density of $j_{\mathrm{NM}} = 8 \times 10^{10}$ A/m^2, the $\theta_{\mathrm{SH}}^{\mathrm{eff}}$ of Ta is determined to be -0.052 ± 0.002 for the up magnetization state and -0.052 ± 0.004 for the down magnetization state. These values are consistent with reported values [31]. Note that the sign of the $\theta_{\mathrm{SH}}^{\mathrm{eff}}$ does not necessarily coincide with that of H_{DL} but is instead governed by the spin Hall conductivity and the polarization direction of the injected spins. Since current shunting between the Ta and CoFeB layers is not considered in this analysis, the extracted $\theta_{\mathrm{SH}}^{\mathrm{eff}}$ values should be regarded as lower bounds. In multilayer structures, differences in resistivity between each layer can lead to significant current shunting, such that the current density in the NM layer (the spin source layer) may differ from the value estimated from the total current density through the entire multilayer. In this case, the exact current density in the NM layer can be estimated by accounting for current shunting using a parallel circuit model [30, 39, 40].

5. Effective Fields of SOT in IMA Systems

Next, we examine harmonic measurements in an in-plane magnetized CoFeB system. First, we derive the $R_{1\omega}$ and $R_{2\omega}$ in bilayer systems with IMA, where the magnetization lies in the xy-plane because of $H_K < 0$. This indicates that the demagnetization field dominates over perpendicular anisotropy, forcing the equilibrium magnetization to align within the film plane. Therefore, it is reasonable to assume that the magnetization direction lies nearly parallel to the film plane ($\theta_0 = \pi/2$), which minimizes the magnetic potential energy. Defining these equilibrium angles is essential for describing SOT components and their angular dependence. Thus, the equilibrium magnetization direction is defined by the following polar and azimuthal angles. The polar angle θ_0 lies in the xy-plane and azimuthal angle φ_0 aligns with the external magnetic field when it is sufficiently larger than the coercivity. Thus, the two angles can be expressed as:

$$\theta_0 = \theta_H = \frac{\pi}{2},\ \varphi_0 = \varphi_H \tag{42}$$

$$\cos\theta_0 = \cos\theta_H = \cos\left(\frac{\pi}{2}\right) = 0,\ \ \sin\theta_0 = \sin\theta_H = \sin\left(\frac{\pi}{2}\right) = 1 \tag{43}$$

Under these approximations and negligible in-plane magnetic anisotropy ($K_{\parallel} \sim 0$), Eq. (7) can be rewritten as:

$$\frac{\partial E}{\partial \theta} = 0 = \left(K_{\perp} - K_{\parallel}\sin^2\varphi_0\right)\sin 2\theta_0 - M_{\mathrm{S}}H \tag{44}$$
$$\left[\cos\theta_0 \sin\theta_H\left(\cos\varphi_0\cos\varphi_H + \sin\varphi_0\sin\varphi_H\right) - \sin\theta_0\cos\theta_H\right]$$

$$\begin{aligned}\frac{\partial E}{\partial \varphi_0} &= 0 = -K_{\parallel}\sin^2\theta_0\sin 2\varphi_0 - M_{\mathrm{S}}H\sin\theta_0\sin\theta_H\sin\left(\varphi_H - \varphi_0\right)\\ &= -K_{\parallel}\sin 2\varphi_0\end{aligned} \tag{45}$$

Substituting Eqs. (44) and (45) into Eqs. (14) and (15) gives

$$\Delta\theta = \frac{\cos\theta_0\left(\Delta H_x\cos\varphi_H + \Delta H_y\sin\varphi_H\right) - \sin\theta_0\Delta H_z}{H_K\cos 2\theta_0 + H\cos\left(\theta_H - \theta_0\right)} = \frac{-\Delta H_z}{-H_K + H} \quad (46)$$

$$\begin{aligned}\Delta\varphi &= \frac{\left(-\Delta H_x\sin\varphi_H + \Delta H_y\cos\varphi_H\right)\cos 2\varphi_H}{H\sin\theta_H}\\ &= \frac{\left(-\Delta H_x\sin\varphi_H + \Delta H_y\cos\varphi_H\right)\cos 2\varphi_H}{H}\end{aligned} \quad (47)$$

By inserting Eqs. (46) and (47) into Eqs. (21) and (22), the $R_{1\omega}$ and $R_{2\omega}$ become

$$R_{1\omega} = \frac{1}{2}\Delta R_{\mathrm{AHE}}\cos\theta_0 + \frac{1}{2}\Delta R_{\mathrm{PHE}}\sin^2\theta_0\sin 2\varphi_H \quad (48)$$

$$R_{2\omega} = -\frac{1}{2}\left[\begin{array}{l}\frac{1}{2}\Delta R_{\mathrm{AHE}}\frac{\Delta H_z}{-H_K + H_{\mathrm{ext}}} + \\ \Delta R_{\mathrm{PHE}}\frac{\left(-\Delta H_x\sin\varphi_H + \Delta H_y\cos\varphi_H\right)\cos 2\varphi_H}{H_{\mathrm{ext}}}\end{array}\right] \quad (49)$$

Note that H is replaced by H_{ext}, indicating the external magnetic field at fixed $\theta_H = \pi/2$.

Eqs. (48) and (49) show that $R_{2\omega}$ is sensitive to ΔH_x, ΔH_y and ΔH_z, corresponding to SOT-induced effective magnetic fields. The H_K in the denominator of the first term of Eq. (49) includes the demagnetization field (H_{dem}) and anisotropy field (H_{ani}), so it can be expressed as:

$$H_K = H_{\mathrm{dem}} - H_{\mathrm{ani}} \quad (50)$$

This H_K can be obtained from AHE curves as shown in Fig. 3(d).

Also, we define H_{DL} and H_{FL} by considering Equation (25). As shown in Fig. 4(b), when the magnetization is parallel to the x-axis, H_{DL} is directed along to the z-direction ($\hat{s} \times \hat{m} = -y \times x$) and H_{FL} is directed along to the y-direction ($-\hat{s}$). Thus, we can separate the terms of Eq. (49) that are related to the τ_{DL} and τ_{FL} terms. The ΔH_z and ΔH_y correspond to the H_{DL} and H_{FL}, respectively. In contrast, ΔH_x is parallel to the magnetization direction and thus generates zero torque ($\hat{m} \times H_x = 0$). Therefore, ΔH_z and ΔH_y are commonly interpreted as H_{DL} and H_{FL}, respectively.

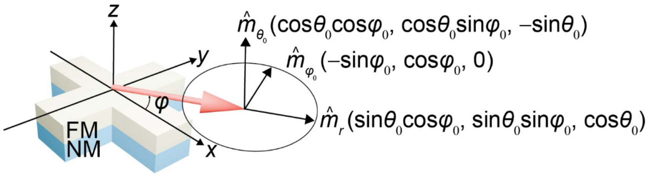

Fig. 6. (Color online) Schematic illustration of the magnetization-centered coordinate system ($\hat{m}_r$, $\hat{m}_{\theta_0}$, $\hat{m}_{\varphi_0}$) in an in-plane magnetized non-magnet (NM)/ferromagnet (FM) bilayer. The magnetization-centered coordinate system can be defined by polar and azimuthal angles (θ_0 and φ_0).

Typically, the SOT of the in-plane magnetized sample is measured by rotating the external magnetic field within the film plane, and therefore the azimuthal angle (φ) dependence of $R_{1\omega}$ and $R_{2\omega}$ is considered. To clearly describe the SOT effective field components as a function of φ, a magnetization-centered coordinate system ($\hat{m}_r$, $\hat{m}_{\theta_0}$, $\hat{m}_{\varphi_0}$) is introduced as shown in Fig. 6. In this coordinate system, $\hat{m}$ represents the equilibrium magnetization direction, $\hat{m}_{\theta_0}$ represents the out of plane direction, and $\hat{m}_{\varphi_0}$ represents the in-plane direction, as shown in Fig. 6. It can be expressed as:

$$\begin{aligned}\hat{m}_r &= \left(\sin\theta_0\cos\varphi_0, \sin\theta_0\sin\varphi_0, \cos\theta_0\right)\\ &= \left(\cos\varphi_0, \sin\varphi_0, 0\right)\end{aligned} \quad (51)$$

$$\hat{m}_{\theta_0} = \left(\cos\theta_0\cos\varphi_0, \cos\theta_0\sin\varphi_0, -\sin\theta_0\right) = \left(0, 0, -1\right) \quad (52)$$

$$\hat{m}_{\varphi_0} = \left(-\sin\varphi_0, \cos\varphi_0, 0\right) \quad (53)$$

This coordinate transformation allows for a clear distinction and interpretation of the effective magnetic field induced by SOT in the IMA system [22]. By redefining the coordinate system relative to the equilibrium magnetization direction, H_{DL} and H_{FL} can be expressed in terms of the orthogonal local axes $\hat{m} \times \hat{y}$ and $\hat{m}_{\varphi_0}$, respectively. This magnetization centered coordinate system enables a clear interpretation of the angular (θ_0, φ_0) dependence of the harmonic Hall resistance and the accurate extraction of each effective field component. By adopting a magnetization centered coordinate transformation, H_{DL} can be expressed as:

$$H_{\mathrm{DL}} = H_{\mathrm{DL}}\left(\hat{m} \times \hat{y}\right) = H_{\mathrm{DL}}^{\theta_0} + H_{\mathrm{DL}}^{\varphi_0} \quad (54)$$

Note that $\hat{m}$ lies in the xy-plane. The projection onto the local axes yields:

$$\begin{aligned}H_{\mathrm{DL}}^{\theta_0} &= H_{\mathrm{DL}}(\hat{m} \times \hat{y}) \cdot H_{\mathrm{FL}}^{\theta_0}\\ &= H_{\mathrm{DL}}(0, 0, \cos\varphi_0) \cdot (0, 0, -1) = H_{\mathrm{DL}}(-\cos\varphi_0)\end{aligned} \quad (55)$$

$$\begin{aligned}H_{\mathrm{DL}}^{\varphi_0} &= H_{\mathrm{DL}}(\hat{m} \times \hat{y}) \cdot \hat{m}_{\varphi_0} = H_{\mathrm{DL}}(0, 0, \cos\varphi_0) \cdot\\ &\quad (-\sin\varphi_0, \cos\varphi_0, 0) = 0\end{aligned} \quad (56)$$

$$H_{\mathrm{DL}} = H_{\mathrm{DL}}^{\theta_0} + H_{\mathrm{DL}}^{\varphi_0} = H_{\mathrm{DL}}(-\cos\varphi_0) \quad (57)$$

Similarly, H_{FL} can be expressed as:

$$H_{\mathrm{FL}} = H_{\mathrm{FL}}[\hat{m} \times (\hat{m} \times \hat{y})] = H_{\mathrm{FL}}^{\theta_0} + H_{\mathrm{FL}}^{\varphi_0} \quad (58)$$

$$\begin{aligned} H_{\mathrm{FL}}^{\theta_0} &= H_{\mathrm{FL}}[\hat{y} - (\hat{m}\cdot\hat{y})\hat{m}]\cdot\hat{m}_{\theta_0} = H_{\mathrm{FL}}(\sin\varphi_0\cos\varphi_0, \\ &\quad \sin^2\varphi_0 - 1, 0)\cdot(0,0,-1) = 0 \end{aligned} \tag{59}$$

$$\begin{aligned} H_{\mathrm{FL}}^{\varphi_0} &= H_{\mathrm{FL}}[\hat{y} - (\hat{m}\cdot\hat{y})\hat{m}]\cdot\hat{m}_{\varphi_0} = \\ &H_{\mathrm{FL}}(\sin\varphi_0\cos\varphi_0, \sin^2\varphi_0 - 1, 0)\cdot(-\sin\varphi_0, \cos\varphi_0, 0) = \\ &H_{\mathrm{FL}}\cos\varphi_0[\sin^2\varphi_0 + \sin^2\varphi_0 - 1] = H_{\mathrm{FL}}(-\cos\varphi_0) \end{aligned} \tag{60}$$

$$H_{\mathrm{FL}} = H_{\mathrm{FL}}^{\theta_0} + H_{\mathrm{FL}}^{\varphi_0} = H_{\mathrm{FL}}(-\cos\varphi_0) \tag{61}$$

Based on these definitions, the ΔH_z and ΔH_y can be expressed in the magnetization-centered coordinate system as:

$$\Delta H_z = H_{\mathrm{DL}}(-\cos\varphi_0) \tag{62}$$

$$\Delta H_y = H_{\mathrm{FL}}\left(-\cos\varphi_0\right) \tag{63}$$

Each effective field exhibits φ angle dependence through the ($-\cos\varphi$) term, indicating that the magnitude of each effective field varies as the magnetization rotates within the film plane. Thus, we obtain an accurate expression for the second harmonic Hall resistance in terms of the angle φ. Also, by simplifying $\cos\varphi\cos2\varphi$ to $2\cos^3\varphi - \cos\varphi$, the angular dependence of $R_{2\omega}$ is obtained:

$$\begin{aligned} R_{2\omega}(\varphi) &= -\frac{1}{2}\left[\frac{1}{2}\Delta R_{\mathrm{AHE}}\frac{H_{\mathrm{DL}}\left(-\cos\varphi_0\right)}{H_{\mathrm{ext}} + H_K} + \Delta R_{\mathrm{PHE}}\frac{H_{\mathrm{FL}}\left(-\cos\varphi_0\right)\cos2\varphi_0}{H_{\mathrm{ext}}}\right] \\ &= \frac{1}{2}\left[\frac{1}{2}\Delta R_{\mathrm{AHE}}\frac{H_{\mathrm{DL}}\cos\varphi_0}{H_{\mathrm{ext}} + H_K} + \Delta R_{\mathrm{PHE}}\frac{H_{\mathrm{FL}}\left(2\cos^3\varphi_0 - \cos\varphi_0\right)}{H_{\mathrm{ext}}}\right] \end{aligned} \tag{64}$$

In addition, we should consider thermal contributions and the Oersted field (H_{Oe}) generated by the injected current because these effects exhibit the same symmetry as H_{DL} and H_{FL}. First, when current is applied to the device, Joule heating occurs, creating a temperature gradient (∇T), primarily perpendicular to the film due to asymmetric heat dissipation between the substrate and air [20, 22, 41, 42]. The thermal gradient is proportional to the square of the current amplitude and the longitudinal sample resistance (R_{xx}), i.e., $\nabla T \propto I^2 R_{xx}$. Under an applied AC current, the time-dependent thermal gradient can be expressed as:

$$\begin{aligned} \nabla T \propto I_0^2\sin^2(\omega t)R_{xx} &= \frac{1}{2}I_0^2[1 - \cos(2\omega t)]R_{xx}, \\ \nabla T &\sim (0, 0, \nabla T_z) \end{aligned} \tag{65}$$

This relationship contains zeroth (DC) and second harmonic (2ω) terms. This ∇T_z can induce both the Anomalous Nernst effect (ANE) and the longitudinal spin Seebeck effect (SSE) [41-44]. The ANE originates from spin dependent electron scattering, generating a voltage difference $V_{\mathrm{ANE}} = -\alpha\nabla T \times \hat{m}$, where α is the ANE coefficient. Its contribution to the $R_{2\omega}$ is expressed as:

$$R_{2\omega}^{\mathrm{ANE}} \propto \nabla T_z \sin\theta\cos\varphi = \nabla T_z \cos\varphi\left(\theta_0 = \frac{\pi}{2}\right) \tag{66}$$

Similarly, the SSE generates a spin current that is converted into a charge voltage through the inverse SHE, given by $V_{\mathrm{SSE}} = S_{\mathrm{SSE}}(\nabla T \times \hat{m})$, where S_{SSE} is the spin Seebeck coefficient. Its contribution to the $R_{2\omega}$ is expressed as:

$$R_{2\omega}^{\mathrm{SSE}} \propto \nabla T_z \sin\theta\cos\varphi = \nabla T_z \cos\varphi\left(\theta_0 = \frac{\pi}{2}\right) \tag{67}$$

Both thermal effects yield $R_{2\omega}$ components proportional to $\cos\varphi$ which are significantly reduced under our measurement condition, exhibiting the same angular symmetry as the H_{DL}. Second, an Oersted field (H_{Oe}) is generated by the current flowing through the NM layer [45]. Its distribution can be derived from the Biot-Savart law, which describes the magnetic field (H) induced by a differential current element:

$$H(r) = \frac{\mu_0}{4\pi}\int\frac{I\mathrm{d}l \times \hat{r}}{r^2} = \frac{\mu_0}{4\pi}\int_{-\infty}^{+\infty}\frac{I\mathrm{d}l \times \hat{r}}{r^2} = \frac{\mu_0 I}{2\pi r} \tag{68}$$

where μ_0 is vacuum permeability, I is current direction and r is distance. It means that the magnetic field is generated in a circular direction (r) surrounding the current (I). Based on Eq. (68), H_{Oe} values at two interfaces can be expressed as:

$$H_{\mathrm{Oe}}^{\mathrm{top}} \approx +\frac{j_{\mathrm{c}} \times t_{\mathrm{NM}}}{2}, \quad H_{\mathrm{Oe}}^{\mathrm{bottom}} \approx -\frac{j_{\mathrm{c}} \times t_{\mathrm{NM}}}{2} \tag{69}$$

According to Eq. (69), the resulting H_{Oe} acts along the same axis as the H_{FL} in the NM/FM bilayers. Therefore, it is essential to carefully distinguish between SOT, thermal, and Oersted field contributions. By incorporating these thermal contributions and H_{Oe} into Eq. (64), the complete $R_{2\omega}(\varphi)$ can be expressed as:

$$R_{2\omega}(\varphi) = \frac{1}{2}\left[\begin{aligned} &\left(\frac{1}{2}\Delta R_{\mathrm{AHE}}\frac{H_{\mathrm{DL}}}{H_{\mathrm{ext}} + H_K} + R_{\nabla T}\right)\cos\varphi_0 \\ &+\left(\Delta R_{\mathrm{PHE}}\frac{H_{\mathrm{FL}} + H_{\mathrm{Oe}}}{H_{\mathrm{ext}}}\right)(2\cos^3\varphi_0 - \cos\varphi_0) \end{aligned}\right] \tag{70}$$

We performed harmonic Hall measurements on a Ta (4 nm)/CoFeB (2 nm) bilayer structure with in-plane magnetization. As shown by Figs. 3(d) and 3(e), the

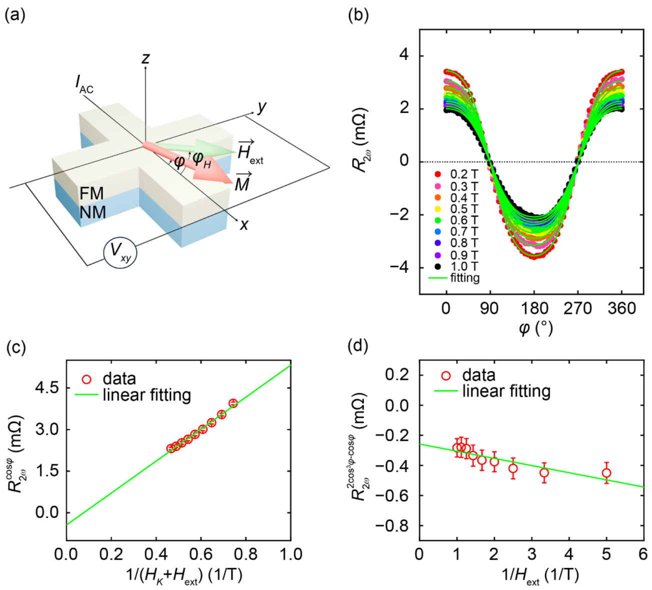

Fig. 7. (Color online) First and second harmonic Hall resistances ($R_{1\omega}$ and $R_{2\omega}$) for the Ta (4 nm)/CoFeB (2 nm) bilayer structure with in-plane magnetic anisotropy. (a) Schematic illustration of the measurement geometry. (b) $R_{2\omega}$ as a function of the azimuthal angle (φ) scan. The colored circles represent measurement data under constant external magnetic field (H_{ext}) of 0.2 T ~ 1.0 T. The green curves indicate fitting lines based on Eq. (70). (c) The cosφ contribution of $R_{2\omega}$ ($R_{2\omega}^{\cos\varphi}$) as a function of $1/(H_K{+}H_{\text{ext}})$. The green line indicates the fitting line obtained from Eq. (71). (d) The $2\cos^3\varphi$-$\cos\varphi$ contribution of $R_{2\omega}$ ($R_{2\omega}^{2\cos^3\varphi-\cos\varphi}$) as a function of $1/(H_{\text{ext}})$. The green line indicates the fitting line obtained from Eq. (72).

measured values are $\Delta R_{\text{AHE}} = 9.5\ \Omega$ and $\Delta R_{\text{PHE}} = 0.88\ \Omega$, respectively. Fig. 7(a) presents the measurement geometry, including angular coordinates and the Hall-bar configuration of the NM/FM bilayer. Fig. 7(b) shows the $R_{2\omega}$ as a function of φ. The applied constant H_{ext} varies from 0.2 T to 1.0 T with a step of 0.1 T. Note that H_{ext} is large enough compared to the coercivity of the CoFeB layer, ensuring $\varphi = \varphi_H = \varphi_0$ in our measurements. To quantitatively evaluate the SOT effective fields, the obtained $R_{2\omega}$ curves are examined by Eq. (70). The fitting curves (solid lines in Fig. 7(b)) separate two terms: a cosφ component ($R_{2\omega}^{\cos\varphi}$), associated with H_{DL} and $R_{\nabla T}$; and a ($2\cos^3\varphi$–$\cos\varphi$) component ($R_{2\omega}^{2\cos^3\varphi-\cos\varphi}$) related to H_{FL} and H_{Oe}.

First, ($R_{2\omega}^{\cos\varphi}$) can be expressed as:

$$R_{2\omega}^{\cos\varphi} \sim \frac{1}{H_K + H_{\text{ext}}} H_{\text{DL}} + R_{\nabla T} \tag{71}$$

In this relation, ($R_{2\omega}^{\cos\varphi}$) and to $1/(H_K + H_{\text{ext}})$ are variables; the slope corresponds to H_{DL} and the intercept represents $R_{\nabla T}$, as shown in Fig. 7(c). The fitted results yield $H_{\text{DL}} = 1.28\pm0.02$ mT and $R_{\nabla T} = -0.16 \pm 0.01$ mΩ.

Second, ($R_{2\omega}^{2\cos^3\varphi-\cos\varphi}$) can be expressed as:

$$R_{2\omega}^{2\cos^3\varphi-\cos\varphi} \sim \frac{1}{H_{\text{ext}}}\left(H_{\text{FL}} + H_{\text{Oe}}\right) \tag{72}$$

Here, ($R_{2\omega}^{2\cos^3\varphi-\cos\varphi}$) and $1/H_{\text{ext}}$ are variables; the slope gives the combined field ($H_{\text{FL}} + H_{\text{Oe}}$), as shown Fig. 7(d). Note that the fitted line is expected to pass through the origin, indicating this term scales with $1/H_{\text{ext}}$. However, a small residual offset remains, which can be attributed to slight misalignment of H_{ext} from the film plane or error in setting the magnetization angle. The H_{Oe} is calculated using Eq. (69) and subtracted from the fitted value. From the fit, ($H_{\text{FL}} + H_{\text{Oe}}$) = −0.13±0.01 mT, H_{Oe} = −0.25 mT, and consequently H_{FL} = 0.12±0.01 mT. The extracted H_{DL} value is substituted into Eq. (28) to determine the $\theta_{\text{SH}}^{\text{eff}}$. Using the saturation magnetization of $M_S = 7.3 \times 10^5$ A/m obtained from VSM measurements and a current density of $j_{\text{NM}} = 10^{11}$ A/m^2, the $\theta_{\text{SH}}^{\text{eff}}$ of Ta is found to be -0.051±0.01. This value is consistent with reported values [46]. Note that this obtained value is a lower bound because current shunting is not considered in this analysis. In multilayer structures, current shunting can cause j_{NM} to deviate from the value estimated simply from the total current. Therefore, the exact j_{NM} can be determined by accounting for current shunting based on the parallel circuit model [30, 39, 40].

6. Conclusion

In this study, we quantitatively evaluated the SOT efficiency in Ta/CoFeB bilayers with different magnetic anisotropies using harmonic Hall measurements. By extracting the H_{DL} and H_{FL}, we determined the $\theta_{\text{SH}}^{\text{eff}}$ to be −0.052±0.002 and −0.052±0.004 for the up and down magnetization states of the perpendicularly magnetized sample, and −0.051±0.001 for the in-plane magnetized sample. These results indicate that the SHE of Ta is an intrinsic property that remains unaffected by the magnetic anisotropy of the FM layer. In addition to the harmonic Hall measurements employed in this study, other techniques such as harmonic Hall measurements under high external magnetic fields in PMA systems [19], ST-FMR [23-27], hysteresis loop shift [28], and current-induced SOT and switching [29-31] can also be utilized to quantitatively evaluate the SOT efficiency. A systematic comparison between these methods is required to quantify the SOT efficiency in various materials accurately. Furthermore, recent studies have reported the emergence of unconventional spin polarizations along the *x* and *z* directions beyond the conventional *y*-

polarized spin current [47-50]. Moreover, the orbital Hall effect and/or the orbital Rashba-Edelstein effect can effectively generate spin torque on the magnetization of the FM layers [30, 31, 51-57]. Therefore, a quantitative approach capable of evaluating and distinguishing these additional spin components and orbital-current-induced torques will be essential for the development of spintronic devices.

Data availability

Data will be made available on request.

Declaration of competing interest

The authors declare that they have no known competing financial interests or personal relationships that could have appeared to influence the work reported in this paper.

Acknowledgements

This work was supported by the National Research Foundation of Korea (RS-2024-00443721, and RS-2025-23323716).

References

[1] V. M. Edelstein, Solid State Commun. **73**, 233 (1990).

[2] J. E. Hirsch, Phys. Rev. Lett. **83**, 1834 (1999).

[3] I. M. Miron, K. Garello, G. Gaudin, P.-J. Zermatten, M. V. Costache, S. Auffret, S. Bandiera, B. Rodmacq, A. Schuhl, and P. Gambardella, Nature **476**, 189 (2011).

[4] L. Liu, C.-F. Pai, Y. Li, H. W. Tseng, D. C. Ralph, and R. A. Buhrman, Science **336**, 555 (2012).

[5] J. Sinova, S. O. Valenzuela, J. Wunderlich, C. H. Back, and T. Jungwirth, Rev. Mod. Phys. **87**, 1213 (2015).

[6] A. Manchon, J. Železný, I. M. Miron, T. Jungwirth, J. Sinova, A. Thiaville, K. Garello, and P. Gambardella, Rev. Mod. Phys. **91**, 035004 (2019).

[7] J. C. Slonczewski, J. Magn. Magn. Mater. **159**, L1 (1996).

[8] L. Berger, Phys. Rev. B **54**, 9353 (1996).

[9] D. C. Ralph and M. D. Stiles, J. Magn. Magn. Mater. **320**, 1190 (2008).

[10] J. Ryu, S. Lee, K.-J. Lee, and B.-G. Park, Adv. Mater. **32**, 1907148 (2020).

[11] M. Cubukcu, O. Boulle, M. Drouard, K. Garello, C.-O. Avci, I. M. Miron, J. Langer, B. Ocker, P. Gambardella, and G. Gaudin, Appl. Phys. Lett. **104**, 042406 (2014).

[12] K. Garello, C.-O. Avci, I. M. Miron, M. Baumgartner, A. Ghosh, S. Auffret, O. Boulle, G. Gaudin, and P. Gambardella, Appl. Phys. Lett. **105**, 212402 (2014).

[13] W. Han, Y. Otani, and S. Maekawa, npj Quantum Mater. **3**, 27 (2018).

[14] R. Ramaswamy, J. M. Lee, K. Cai, and H. Yang, Appl. Phys. Rev. **5**, 031107 (2018).

[15] C. Song, R. Zhang, L. Liao, Y. Zhou, X. Zhou, R. Chen, Y. You, X. Chen, and F. Pan, Prog. Mater. Sci. **118**, 100761 (2021).

[16] U. H. Pi, K. W. Kim, J. Y. Bae, S. C. Lee, Y. J. Cho, K. S. Kim, and S. Seo, Appl. Phys. Lett. **97**, 162507 (2010).

[17] J. Kim, J. Sinha, M. Hayashi, M. Yamanouchi, S. Fukami, T. Suzuki, S. Mitani, and H. Ohno, Nat. Mater. **12**, 240 (2013).

[18] K. Garello, I. M. Miron, C.-O. Avci, F. Freimuth, Y. Mokrousov, S. Blügel, S. Auffret, O. Boulle, G. Gaudin, and P. Gambardella, Nat. Nanotechnol. **8**, 587 (2013).

[19] X. Qiu, P. Deorani, K. Narayanapillai, K.-S. Lee, K.-J. Lee, H.-W. Lee, and H. Yang, Sci. Rep. **4**, 4491 (2014).

[20] M. Hayashi, J. Kim, M. Yamanouchi, and H. Ohno, Phys. Rev. B **89**, 144425 (2014).

[21] C.-O. Avci, K. Garello, C. Nistor, S. Godey, B. Ballesteros, A. Mugarza, A. Barla, M. Valvidares, E. Pellegrin, A. Ghosh, I. M. Miron, O. Boulle, S. Auffret, G. Gaudin, and P. Gambardella, Phys. Rev. B **89**, 214419 (2014).

[22] C.-O. Avci, K. Garello, M. Gabureac, A. Ghosh, A. Führer, S. F. Alvarado, and P. Gambardella, Phys. Rev. B. **90**, 224427 (2014).

[23] L. Liu, T. Moriyama, D. C. Ralph, and R. A. Buhrman, Phys. Rev. Lett. **106**, 036601 (2011).

[24] C.-F. Pai, L. Liu, Y. Li, H. W. Tseng, D. C. Ralph, and R. A. Buhrman, Appl. Phys. Lett. **101**, 122404 (2012).

[25] A. Ganguly, K. Kondou, H. Sukegawa, S. Mitani, S. Kasai, Y. Niimi, Y. Otani, and A. Barman, Appl. Phys. Lett. **104**, 072405 (2014).

[26] Y. Wang, P. Deorani, X. Qiu, J. H. Kwon, and H. Yang, Appl. Phys. Lett. **105**, 152412 (2014).

[27] W. Zhang, W. Han, X. Jiang, S.-H. Yang, and S. S. P. Parkin, Nat. Phys. **11**, 496 (2015).

[28] C.-F. Pai, M. Mann, A. J. Tan, and G. S. D. Beach, Phys. Rev. B **93**, 144409 (2016).

[29] R. Mishra, J. Yu, X. Qiu, M. Motapothula, T. Venkatesan, and H. Yang, Phys. Rev. Lett. **118**, 167201 (2017).

[30] S. Lee, M.-G. Kang, D. Go, D. Kim, J.-H. Kang, T. Lee, G.-H. Lee, J. Kang, N. J. Lee, Y. Mokrousov, S. Kim, K.-J. Kim, K.-J. Lee, and B.-G. Park, Commun. Phys. **4**, 234 (2021).

[31] S. y. Shin, D. Han, S. Lee, and B.-G, Park. Adv. Func. Mater. **35**, 2425932 (2025).

[32] L. Landau and E. Lifshitz, Phys. Z. Sowjetunion **8**, 153 (1935).

[33] T. L. Gilbert, IEEE Trans. Magn. **40**, 3443 (2004).

[34] Y. Tserkovnyak, A. Brataas, and G. E. W. Bauer, Phys. Rev. B **66**, 224403 (2002).

[35] C. T. Boone, H. T. Nembach, J. M. Shaw, and T. J. Silva, J. Appl. Phys. **113**, 153906 (2013).

[36] H. Jiao and G. E. W. Bauer, Phys. Rev. Lett. **110**, 217602 (2013).

[37] J.-C. Rojas-Sánchez, N. Reyren, P. Laczkowski, W. Savero, J. P. Attané, C. Deranlot, M. Jamet, J.-M. George, L. Vila, and H. Jaffrès, Phys. Rev. Lett. **112**, 106602 (2014).

[38] L. Zhu, D. C. Ralph, and R. A. Buhrman, Appl. Phys. Rev. **8**, 031308 (2021).

[39] L. Zhu, D. C. Ralph, and R. A. Buhrman, Phys. Rev. Appl. **10**, 031001 (2018).

[40] L. Huang, S. He, Q. J. Yap, and S. T. Lim, Appl. Phys. Lett. **113**, 022402 (2018).

[41] K. Uchida, S. Takahashi, K. Harii, J. Leda, W. Koshibae, K. Ando, S. Maekawa, and E. Saitoh, Nature. **455**, 778 (2008).

[42] G. E. W. Bauer, E. Saitoh, and B. J. van Wees, Nat Mater. **11**, 391 (2012).

[43] S. Beckert, J. Godinho, F. Johnson, J. Kimák, E. Schmoranzerová, J. Zemen, Z. Šobáň, K. Olejník, J. Železný, J. Wunderlich, P. Němec, D. Kriegner, A. Thomas, S. T. B. Goennenwein, L. F. Cohen, and H. Reichlová, Phys. Rev. B. **108**, 024420 (2023).

[44] T.-C. Chuang, P.-L. Su, P.-H. Wu, and S.-Y. Huang, Phys. Rev. B. **96**, 174406 (2017).

[45] T. D. Skinner, M. Wang, A. T. Hindmarch, A. W. Rushforth, A. C. Irvine, D. Heiss, H. Kurebayashi, and A. J. Ferguson, Appl. Phys. Lett. **104**, 062401 (2014).

[46] Z. Zhang, J. Zhang, Z. Weng, J. Li, H. Song, and W. Lin, Phys. Rev. B. **111**, 104412 (2025).

[47] Y. Liu, G. Shi, D. Kumar, T. Kim, S. Shi, D. Yang, J. Zhang, C. Zhang, F. Wang, X. Yang, Y. Pu, P. Yu, K. Cai, and H. Yang, Nat. Electron. **6**, 732 (2023).

[48] M. Wang, Y. Tao, T. Xiong, D. Wu, S. Zhao, Y. Li, Z. Wang, Y. Liu, C. Wang, T. Song, Q. Wang, J. Wang, Y. Chen, Z. Ma, B. Li, Z. Li, X. Lin, Z. Zhou, X. Li, F. Hu, H. Yu, Q. Zhang, and X. Han, Nat. Commun. **14**, 2871 (2023).

[49] G. Zeng, Y. Zhang, L. Xu, P. Zhang, C. Cao, Y. Liu, R. Xiong, S. Chen, and S. Liang, Phys. Rev. Appl. **24**, 044086 (2025).

[50] M.-G. Kang, S. Lee, and B.-G. Park, npj Spintronics. **3**, 8 (2025).

[51] S. Ding, A. Ross, D. Go, L. Baldrati, Z. Ren, F. Freimuth, S. Becker, F. Kammerbauer, J. Yang, G. Jakob, Y. Mokrousov, and M. Kläui, Phys. Rev. Lett. **125**, 177201 (2020).

[52] D. Lee, D. Go, H.-J. Park, W. Jeong, H.-W. Ko, D. Yun, D. Jo, S. Lee, G. Go, J. H. Oh, K.-J. Kim, B.-G. Park, B.-C. Min, H.-C. Koo, H.-W. Lee, O. Lee, and K.-J. Lee, Nat. Commun. **12**, 6710 (2021).

[53] J. Kim, D. Go, H. Tsai, D. Jo, K. Kondou, H.-W. Lee, and Y. Otani, Phys. Rev. B. **103**, L020407 (2021).

[54] T. Gao, P. Rüßmann, Q. Wang, R. Fukunaga, H. Hayashi, D. Go, T. Harumoto, R. Tu, S. Zhang, L. Zhang, Y. Mokrousov, J. Shi, and K. Ando, Nat. Phys. **20**, 1896 (2024).

[55] Z. Zhu, L. Cheng, X. Xu, K. Meng, J. Zhang, X. Deng, T. Zhu, H. Lv, R. Che, D. Shao, D. Zhang, Y. Wu, G. Zhang, and Y. Jiang, Adv. Mater. **37**, 2418264 (2025).

[56] W. Kim, G. Jung, D. Woo, S. Yoon, and S. Lee, J. Korean Magn. Soc. **35**, 86 (2025).

[57] R. Gupta, C. Bouard, F. Kammerbauer, J. O. Ledesma-Martin, A. Bose, I. Kononenko, S. Martin, P. Usé, G. Jakob, M. Drouard, and M. Kläui, Nat. Commun. **16**, 130 (2025).